Simulation of defects in CFRP and delayed TR-NEWS analysis

Research Report Mech 320/17

M. Lints[1,2], A. Salupere[1], S. Dos Santos[2]

[1] Tallinn University of Technology, Department of Cybernetics,
Akadeemia tee 21, 12618 Tallinn, Estonia
[2] INSA Centre Val de Loire, Blois Campus;
COMUE "Léonard de Vinci", U930 "Imagerie et Cerveau" Inserm,
3 rue de la Chocolaterie, CS23410, 41034 Blois, France

Contents

1 Introduction

In the past, the use of carbon fibre reinforced polymer (CFRP) has been limited to non-structural parts of high-tech aeronautical products. In recent times, due to the effort of weight reduction and product lifetime enhancement, the application areas of CFRP have widened to the load-bearing parts of the aeronautical, automotive and civil engineering products. Due to the increased demands on the strength of the CFRP products and possible complex failure mechanisms, the Non-Destructive Testing (NDT) methods of CFRP have been an important applied and academic problem.

The complex failure mechanisms of CFRP include microcracking and delamination. Microcracking can occur at lower loads or due to aging and can be difficult to examine using ultrasonic NDT. With increased loading, the damage can evolve to delaminations, a very fine cracking between the layers of the CFRP. These damages are difficult to detect using ultrasonic methods due to their small thicknesses. The damage can exhibit itself as a contact acoustical nonlinearity [1]. A statistical distribution of microcracks or delamination damage in the material could also be described by hysteresis in a continuum material model [2, 3, 4]. This can also be applicable for other materials than CFRP, for example biological tissues [5, 6].

This research report explores the possibility of using the nonlinear effects of a single small crack, which can come into contact with itself, much like the contact acoustical nonlinearity. Its effect on the ultrasonic wave propagation is examined using Finite Element simulations. The goal of this research report is to describe in length the simulation code and the initial result analysis. The simulation results are analysed using Pulse Inversion (PI) [7], spectral analysis and delayed TR-NEWS [8] to detect the effect of the damage in simulation model, as a source of nonlinear effects. The effectiveness of these methods have been shown by numerical simulations and physical experiments in previous work [8]. In this work, the Finite Element Method (FEM) model is advanced further by including absorbing boundary conditions and the contacting crack defect in the material.

2 Experiment and simulation configuration

This section describes the physical experiment on which the simulation is based, and describes the differences and similarities between the simulation and the experiment.

2.1 Test object in physical experiment

The test object is a CFRP block consisting of 144 layers (Fig. 1). It is composed of fabric woven from yarns of fibre and impregnated with epoxy. The cross-section of the yarns have elliptical shape (Fig. 2) and the material has inclusions of pure epoxy, so a wave propagating through the material will encounter yarns (fibres with epoxy) and areas of pure epoxy. A simple material model for this test object is the laminate model (Fig. 3) where: i) the material consists of homogeneous layers, ii) each layer has its own elasticity properties, and iii) dispersion arises due to the periodical discontinuity of the material properties.

The material in the simulation was modelled as laminate of three different kind of layers with different mechanical properties:

- pure epoxy layer as an isotropic material: $E = 3.7$ GPa, $\nu = 0.4$, $\rho = 1200$ kg/m^3,

- composite with fabric at 0/90° direction as transversely isotropic material: $E_1 = E_2 = 70$ GPa, $G_{12} = 5$ GPa, $\nu_{12} = 0.1$, $\rho = 1600$ kg/m^3,

- composite with fabric at 45°/45° direction as transversely isotropic material: $E_1 = E_2 = 20$ GPa, $G_{12} = 30$ GPa, $\nu_{12} = 0.74$, $\rho = 1600$ kg/m^3.

Figure 1: Carbon Fibre Reinforced Polymer (CFRP) block in the test configuration with transmitting transducer on side and receiving on top
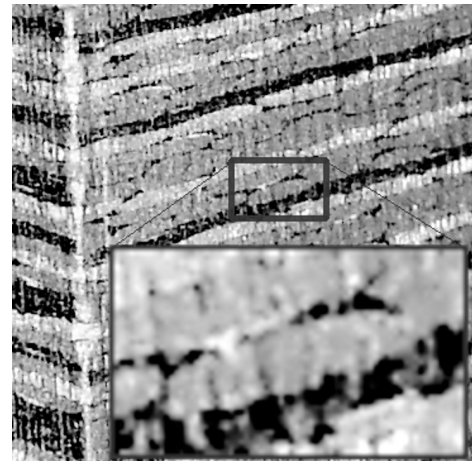

Figure 2: The layered structure of the CFRP with the fabric yarns in tight packing and epoxy filling the voids

The simulations reflect the actual physical experiments as closely as possible. In the physical experiments, the CFRP block (Fig. 1) was studied using TR-NEWS NDT equipment and signal processing methods. The simulations echo the physical experiments in terms of the transducer placement, frequencies and signal processing. Conversely, the simulations differ from the physical experiments in the sense that: i) the wave energy is introduced into the material without losses, ii) the material is simulated in 2D instead of 3D, and iii) only the relevant part of the object of it is modelled (region near and between the transducers). Absorbing boundary conditions allow the wave propagation out of the region of interest.

In the physical experiment, the CFRP block was excited from its side with 20° shear wave transducer. The signal was received with a plane wave transducer on the top of the block (Fig. 3). The test equipment consisted of:

Preamplifier Juvitek TRA-02 (0.02 - 5 MHz) connected to a computer,

Amplifier ENI model A150 (55 dB at 0.3-35 MHz),

Shear wave transducer Technisonic ABFP-0202-70 (2.25 MHz),

Longitudinal wave transducer Panametrics V155 (5 MHz).

The roles of the transducers are not changed during the experiment: the focusing of the ultrasonic wave relies on the TR-NEWS signal processing. This is a two-pass method where the receiving and transmitting transducers do not change their roles. In this sense the "Time Reversal" describes the signal processing method which accounts for internal reflections of the material as virtual transducers, used for focusing the wave in the second pass of the wave transmission. The placement of the transducers is otherwise not important: in NDT investigation they could be placed arbitrarily and they do not have to be in line with each other, but the configuration must remain fixed during the complete TR-NEWS procedure. The signal processing steps are explained in Section 3.

2.2 The simulation model

The simulation is in time domain only, since the TR-NEWS procedure relies on transient echoes and complex wave motion for the wave energy focusing process. Due to the heavy computational cost of time domain simulation, a simple laminate model is used to describe CFRP. It consists of CFRP layers with $90°/0°$ weave, $45°/45°$ weave and epoxy layer. The thicknesses of the layers are given by functions of random variables which reflect the actual structure of the material. The random variable distribution is measured from a close-up image of the CFRP test object.

2.2.1 Layered model of the material

In this work, the CFRP block is described as a laminate made of different anisotropic but periodically occurring layers of various thicknesses. This introduces some degree of dispersion and reverberation into the model, which also exists in the real material. If the magnitude of the nonlinearity matches the dispersion, then solitary waves may emerge. Reverberation in the material happens due to interfaces between different materials. Reverberations in the undamaged material are usually considered unwanted in NDT applications, but TR-NEWS signal processing actually relies on the internal echoes for the focusing of the pulse. The internal echoes or "virtual transducers" [9] capture and release the transient wave energy in different directions. Using TR-NEWS signal processing, these "virtual transducers" can be made to reverberate so to create a wave focusing in one predetermined place and time in the material.

The thicknesses of the layers of the model reflect the actual structure with tightly packed carbon fibre yarns and epoxy. It is assumed that the yarn ellipse semi-axis dimensions follow the normal distribution. Therefore the yarn size distribution can be measured from the close-up image of the CFRP block, results of which are given in the Table 1. The transformation of pixels to millimetres in the image is 48.27 ± 14 px/mm, making the standard uncertainty of measuring length by pixels 8.1 px/mm. With confidence of 95% the width of the average yarn is 1.50 ± 0.26 mm and the height is 0.261 ± 0.051 mm.

We have the following procedure for creating the model of the CFRP with stochastic layer thicknesses (Fig. 3), reflecting the randomness of the thicknesses of pure yarn and epoxy encountered by a wave propagating through the block. In creating the model we "freeze" the

Table 1: Dimensions of yarns measured from image

No.	width, px	height, px
1	72	14
2	69	14
3	70	13
4	72	13
5	78	12
6	75	13
7	70	13
8	75	11
9	71	10
Mean	72.4	12.6
Std dev	2.8	1.3

dimensions of ellipses (semi-axes a and b) and pack the ellipses. Knowing the semi-axes a and b of the ellipses and that all ellipses are identical, then the representative element in tight packing looks like shown in Fig. 4, containing two quarters of an ellipse. The formula for ellipse is

$$\frac{x^2}{a^2} + \frac{y^2}{b^2} = 1. \tag{1}$$

If the packed ellipses have equal size, then their horizontal distance is a. Therefore the ellipses touch at midpoint $x = a/2$ of the representative element and we substitute the midpoint into the ellipse formula to find the half-height of the representative element. Therefore in tight packing the vertical distance between the ellipses is twice the thickness of the quarter ellipse at $x = a/2$ in Fig. 4, expressed by

$$\frac{a^2}{4a^2} + \frac{y^2}{b^2} = 1 \quad \Rightarrow \quad y = \frac{\sqrt{3}}{2}b. \tag{2}$$

Consequently the offset between identical ellipses for maximum packing is $(a, \sqrt{3}b)$. We can express $y(x)$ for a single quarter of ellipse as

$$y(x) = \frac{b}{a}\sqrt{a^2 - x^2}. \tag{3}$$

Due to the symmetry of top and bottom quarter-ellipse (solid and dotted lines in Fig. 4), the vertical thickness of CFRP yarn portion in the representative element is given by

$$f_C(x) = y(x) + y(a - x) = \frac{b}{a}\left(\sqrt{a^2 - x^2} + \sqrt{2ax - x^2}\right). \tag{4}$$

Full height of the two packed quarters $\sqrt{3}b$ minus the thickness of the CFRP portion $f_C(x)$ gives the thickness of epoxy part between the ellipse quarters

$$f_E(x) = \sqrt{3}b - f_C(x). \tag{5}$$

Semi-axes of the ellipse $a = \mathcal{N}(\mu_a, \sigma_a^2)$ and $b = \mathcal{N}(\mu_b, \sigma_b^2)$ are normal random variables found from the distribution of carbon fibre ellipses in real material (Fig. 2). Therefore the computational model reflects the actual material due to the randomness of the layer thicknesses
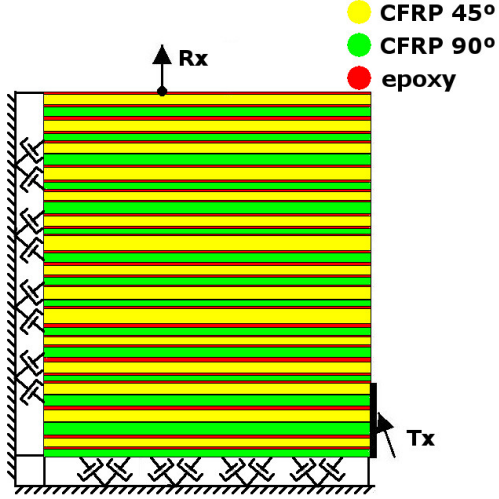
Figure 3: The laminate material model with layers of stochastic thicknesses and absorbing boundary conditions on bottom and left boundaries and four fixed degrees of freedom
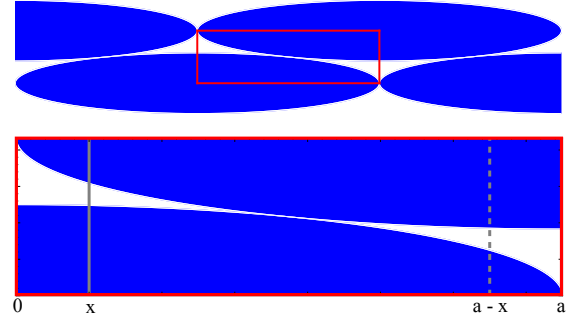

Figure 4: Ellipsoidal yarns in tight packing resulting in a representative element with two quarters of ellipse

being in accordance with the ellipses in actual CFRP block. Uniform random variable $x = \mathcal{U}(0, a)$ is a function of geometric probability which describes where along the ellipse semi-major axis the wave passes through the ellipse (Fig. 4).

In short, the following steps are used for creating the laminate model shown in Fig. 3. It has stochastic layer thicknesses, reflecting the randomness of the thicknesses of pure yarn and epoxy encountered by a wave propagating through the block. Assuming that we know the random distribution of the dimensions of yarn ellipses, we have the following procedure for each pair of pure CFRP yarn and pure epoxy layers in a representative element (Fig. 4).

1. Find the semi-axis dimensions of an ellipse a and b as random variables of the known normal distribution (distribution is found by analysing the structure of the actual material).

2. Find a random location $x \in [0, a]$, as element of uniform distribution, for the wave to pass through the representative element.

3. Using found values of random variables a, b and x, find the thickness of pure CFRP and pure epoxy (Eqs. (4) and (5)) encountered by the wave.

4. As a practical aspect, the thickness of the pure epoxy layer must not be too small, as it can prohibit the generation of a good FEM mesh.

The laminate model was constructed by finding the semi-major axis length a (where mean $\mu_a = 0.750$ mm, dispersion $\sigma_a = 0.130$ mm) and semi-minor axis length b (where mean $\mu_b = 0.130$ mm, dispersion $\sigma_b = 0.025$ mm) and wave traversing location $x \in [0, a]$ as random variables for a pair of layers (composite and epoxy). The physical properties of the composite fabric direction (90° or 45°) alternated for each pair (Fig. 3). The simulation model consisted of 50 such pairs which were generated and stacked together.

3 TR-NEWS signal processing

Figure 5 outlines the TR-NEWS signal processing steps. The simulation uses the same signal processing steps as are usually applied to physical experiments. Firstly the chirp-coded excitation $c(t)$ is transmitted through the medium.

$$c(t) = A \cdot \sin\left(\psi(t)\right), \tag{6}$$

where $\psi(t)$ is linearly changing instantaneous phase. In this work, a sweep from 0 to 2 MHz was used. Then the chirp-coded coda response $y(t)$ with a time duration T is recorded

$$y(t,T) = h(t) * c(t) = \int_{\mathbb{R}} h(t - t', T)c(t')dt', \tag{7}$$

where $h(t - t', T)$ is the impulse response of the medium. The $y(t,T)$ is the direct response from the receiving transducer when the chirp excitation $c(t)$ is transmitted through medium. Next the correlation $\Gamma(t)$ between the received response $y(t,T)$ and chirp-coded excitation $c(t)$ is computed during some time period Δt

$$\Gamma(t) = \int_{\Delta t} y(t - t', T)c(t')dt' \simeq h(t) * c(t) * c(T - t, T), \tag{8}$$

where the $h(t) * c(t) * c(T - t, T)$ is pseudo-impulse response which is proportional to the impulse response $h(t)$ if using linear chirp excitation for $c(t)$ because $\Gamma_c(t) = c(t) * c(T - t) = \delta(t - T)$. Therefore the actual correlation $\Gamma(t) \sim h(t)$ contains information about the wave propagation paths in complex media.

Time reversing the correlation $\Gamma(t)$ from the previous step results in $\Gamma(-t)$ used as a new input signal. Re-propagating $\Gamma(-t)$ in the same configuration as the initial chirp yields

$$y_{TR}(t, T) = \Gamma(T - t) * h(t) \sim \delta(t - T), \tag{9}$$

where $y_{TR} \sim \delta(t - T)$ is now the focused signal under receiving transducer where the focusing takes place at time T. This is because $\Gamma(t)$ contains information about the internal reflections of the complex media. Transmitting its time reversed version $\Gamma(T - t)$ will eliminate these reflection delays by the time signal reaches the receiver, resulting in the focused signal y_{TR} (Eq. (9)). The test configuration must remain constant during all of these steps, otherwise the focusing is lost. The steps of this focusing process in a physical experiment are shown in Fig. 6.

3.1 Delayed TR-NEWS

Delayed TR-NEWS signal processing considers a single y_{TR} focusing wave as a new basis which can be used to build arbitrary wave shapes at the focusing. This is done by time-delaying and superimposing n time-reversed correlation $\Gamma(T - t)$ signals (Fig. 7 left column)

$$\Gamma_s(T - t) = \sum_{i=0}^{n} a_i \Gamma(T - t + \tau_i) = \sum_{i=0}^{n} a_i \Gamma(T - t + i\Delta\tau), \tag{10}$$

where a_i is the i-th amplitude coefficient and τ_i the i-th time delay. In case of uniform time delay the $\Delta\tau$ is the time delay between samples. Upon propagating this $\Gamma_s(t - T)$ through the media according to the last step of TR-NEWS, a delayed scaled shape of signal at the focusing
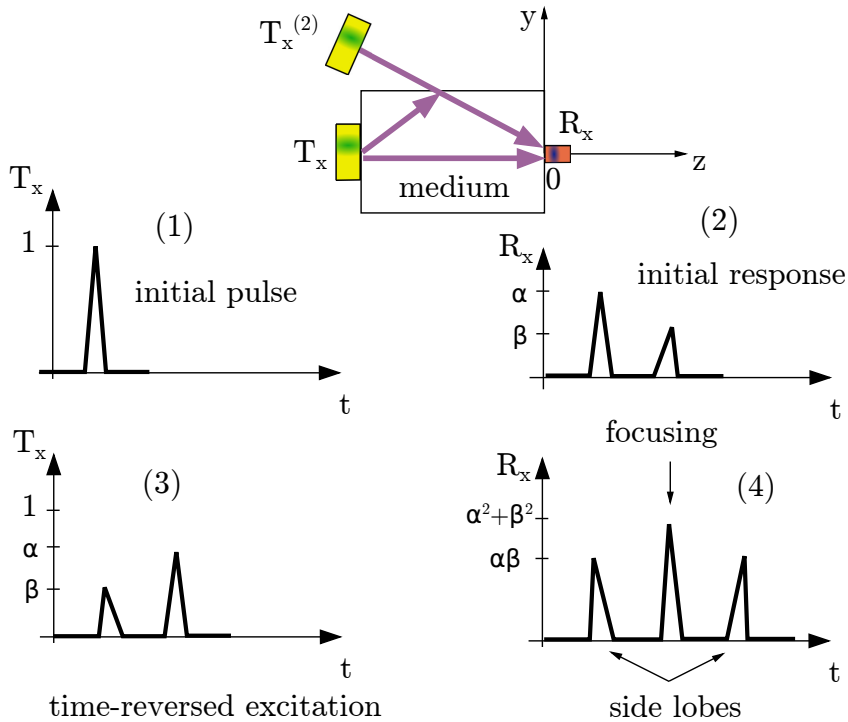
Figure 5: Schematic process of TR-NEWS with the virtual transducer concept. (1) The initial broadband excitation $T_x(t)$ propagates in a medium. (2) Additional echoes coming from interfaces and scatterers in its response R_x could be associated to a virtual source $T_x^{(2)}$. (3) Applying reciprocity and TR process to R_x. (4) The time reversed new excitation $T_x = R_x(-t)$ produces a new response R_x (the TR-NEWS coda $y_{TR}(t)$) with a spatio-temporal focusing at $z = 0; y = 0; t = t_f$ and symmetric side lobes with respect to the focusing.

point can be created. The delayed TR-NEWS signal processing optimization can be used for amplitude modulation, signal improvement and sidelobe reduction [8].

It is possible to predict what the delayed TR-NEWS focusing output would be in a linear material (Fig. 7 right column):

$$y_{dTR}(t) = \left[\sum_i a_i \Gamma_c \left(T - t + \tau_i \right) \right] * h(t) \quad \overset{\text{linearity}}{=\!=\!=\!=\!=\!=}$$

$$= \sum_i a_i \Gamma_c \left(T - t + \tau_i \right) * h(t) = \sum_i a_i y_{TR}(t - \tau_i). \quad (11)$$

The purpose of the prediction is twofold. Firstly it can be used to figure out optimal delay and amplitude parameters a_i and τ_i for delayed TR-NEWS experiment, using the original focusing peak y_{TR}. Secondly it could be possible to analyse the differences between the measured delayed TR-NEWS result and its prediction. The difference could indicate the magnitude of nonlinearity, because the prediction relies on the applicability of linear superposition and is found to be quite accurate in experiments with linear material [8].

4 Finite element model

The simulation program considers 2D wave propagation in a solid material with linear elasticity. The nonlinearity comes from an internal defect, a crack in the computational region which can
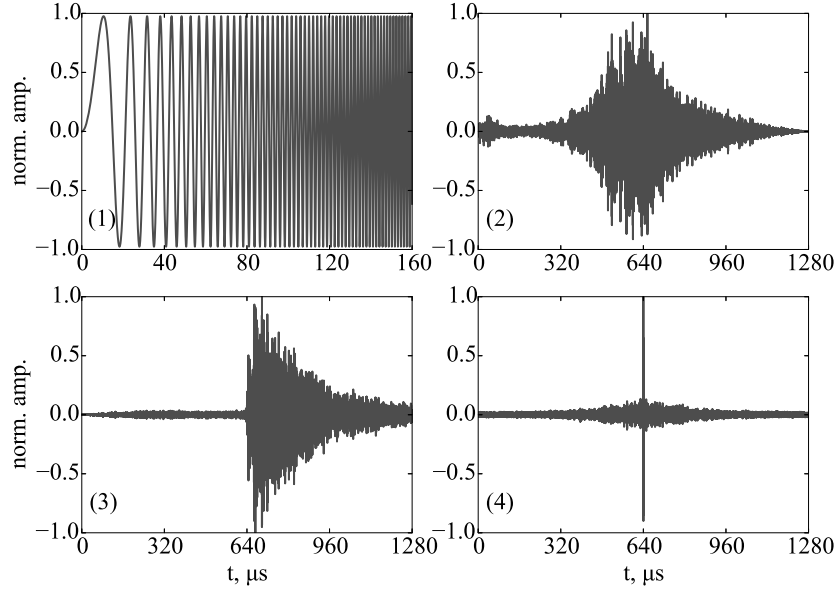
Figure 6: Bi-layered aluminium experimental chirp-coded TR-NEWS signal processing steps: (1) chirp excitation, (2) output recorded at Rx, (3) cross-correlation between input and output, (4) focusing resulting from taking time-reversed cross-correlation as new input [8].
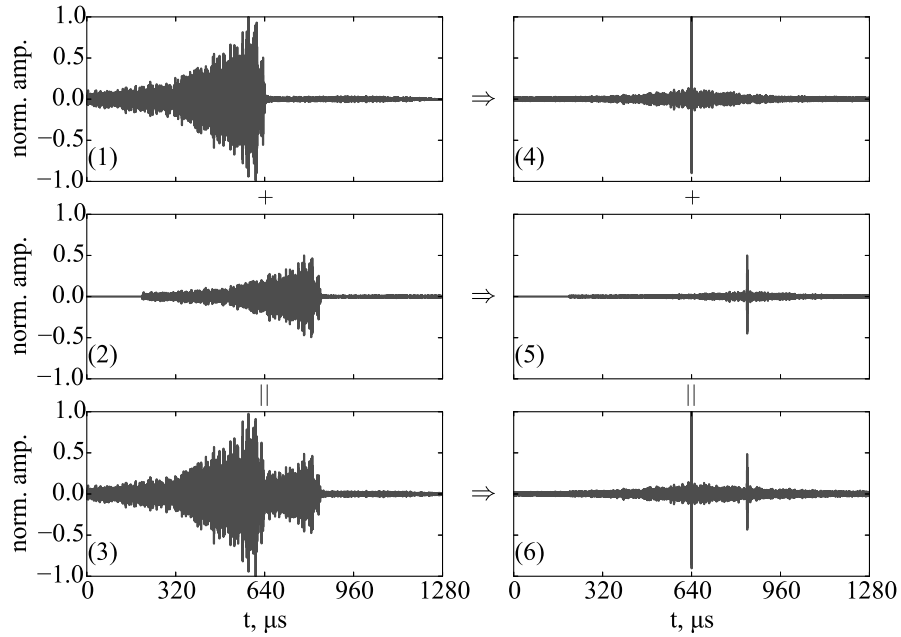
Figure 7: Delayed TR-NEWS signal processing steps in bi-layered aluminium, starting from the cross-correlation step (left column) and prediction of linear superposition of waves (right column): (1) cross-correlation(Eq. (8)), (2) delayed and scaled cross-correlation, (3) linear superposition of two cross-correlations which becomes the new excitation, (4) focusing (Eq. (9)), (5) delayed and scaled focusing, (6) linear superposition of the two focusing peaks.

come into contact with itself. This contacting nonlinearity has asymmetric stiffness and is therefore nonclassically nonlinear. Since the CFRP is a complex material, then in this work it is modelled as a laminate with anisotropic layers arranged in a periodic manner, described in Section 2.2.1. Because the physical experiment was conducted on the corner of a large CFRP block, the simulation is also in a semi-infinite quarter-space. The region has two free surfaces and two absorbing boundaries for the wave energy to escape.

The constitutive equation of the material itself is linear (although anisotropic), therefore the logic follows Reddy [10]. The linear elastodynamics problem is solved

$$\rho \ddot{u}_i - \sigma_{ij,j} = b_i, \tag{12}$$

where ρ is material density, u_i is displacement component, σ_{ij} is stress component, and b_i is body force component. Einstein summation convention is used and comma in index denotes spatial derivative. The constitutive equation in the variational formulation is

$$0 = \int_{\Omega} \left(\sigma_{ij} \delta\varepsilon_{ij} + \rho \ddot{u}_i \delta u_i \right) dxdy - \int_{\Omega} b_i \delta u_i dxdy - \int_{\Gamma} t_i \delta u_i ds \tag{13}$$

where ε_{ij} is strain and t_i is traction component on boundary. In our case the region Ω is a 2D space and boundary Γ surrounding it is a 1D line. The body forces are zero in this simulation. Strain is assumed to be small. The variational formulation in Eq. (13) is suitable for using with FEniCS or a similar multiphysics program. For hand-programmed calculations the equations need to be written in a matrix form, expressed using shape functions and assembled into global matrices. The simulation programs are written using SciPy Python package [11].

The variational formulation (Eq. (13)) can be used directly to write out the FEM formulas. Alternatively the linear elastodynamics problem (Eq. (12)) can be used to arrive to the weak formulation by: i) writing out the equations of motion, ii) multiplying them by a weight function, iii) integrating over the element volume, and iv) integration by parts using the divergence theorem to separate the boundary conditions and arrive at the weak form for an element [10]. Equation (12) can be written for 2D case as

$$\begin{cases} \frac{\partial \sigma_{xx}}{\partial x} + \frac{\partial \sigma_{xy}}{\partial y} + b_x = \rho \frac{\partial^2 u_x}{\partial t^2} \\ \frac{\partial \sigma_{xy}}{\partial x} + \frac{\partial \sigma_{yy}}{\partial y} + b_y = \rho \frac{\partial^2 u_y}{\partial t^2} \end{cases}, \tag{14}$$

where $\sigma_{xy} = \sigma_{yx}$. Proceeding with Galerkin method by multiplying the equations with a shape functions w_1 and w_2 and integrating over a volume, the equations become

$$\begin{cases} \int_{\Omega} \left(w_1 \frac{\partial \sigma_{xx}}{\partial x} + w_1 \frac{\partial \sigma_{xy}}{\partial y} + w_1 b_x - w_1 \rho \frac{\partial^2 u_x}{\partial t^2} \right) dxdy = 0 \\ \int_{\Omega} \left(w_2 \frac{\partial \sigma_{xy}}{\partial x} + w_2 \frac{\partial \sigma_{yy}}{\partial y} + w_2 b_y - w_2 \rho \frac{\partial^2 u_y}{\partial t^2} \right) dxdy = 0 \end{cases}. \tag{15}$$

The equations are converted to weak form by using 2D integration by parts

$$\int_{\Omega} w \frac{\partial G}{\partial x_l} dxdy = \int_{\Gamma} n_{x_l} w G ds - \int_{\Omega} \frac{\partial w}{\partial x_l} G dxdy, \tag{16}$$

where G is a scalar function defined in 2D domain Ω, l denotes the coordinate index and n_l is the normal vector component in the l coordinate direction. This reduces the order of the derivative by moving it to the weight function and exposing the boundary conditions. So using

Eq. (16) in Eq. (15) we get

$$
\begin{cases}
\int_\Gamma w_1 \sigma_{xx} n_x ds - \int_\Omega \frac{\partial w_1}{\partial x} \sigma_{xx} dx dy + \int_\Gamma w_1 \sigma_{xy} n_y ds - \int_\Omega \frac{\partial w_1}{\partial y} \sigma_{xy} dx dy + \\
+ \int_\Omega w_1 b_x dx dy - \int_\Omega \rho w_1 \frac{\partial^2 u_x}{\partial t^2} dx dy = 0, \\
\int_\Gamma w_2 \sigma_{xy} n_x ds - \int_\Omega \frac{\partial w_2}{\partial x} \sigma_{xy} dx dy + \int_\Gamma w_2 \sigma_{yy} n_y ds - \int_\Omega \frac{\partial w_2}{\partial y} \sigma_{yy} dx dy + \\
+ \int_\Omega w_2 b_y dx dy - \int_\Omega \rho w_2 \frac{\partial^2 u_y}{\partial t^2} dx dy = 0,
\end{cases}
\tag{17}
$$

which can be gathered into

$$
\begin{cases}
\int_\Omega \left(\rho w_1 \frac{\partial^2 u_x}{\partial t^2} + \frac{\partial w_1}{\partial x} \sigma_{xx} + \frac{\partial w_1}{\partial y} \sigma_{xy} \right) dx dy - \int_\Omega w_1 b_x dx dy - \int_\Gamma w_1 t_x ds = 0, \\
\int_\Omega \left(\rho w_2 \frac{\partial^2 u_y}{\partial t^2} + \frac{\partial w_2}{\partial x} \sigma_{xy} + \frac{\partial w_2}{\partial y} \sigma_{yy} \right) dx dy - \int_\Omega w_2 b_y dx dy - \int_\Gamma w_2 t_y ds = 0,
\end{cases}
\tag{18}
$$

where tractions $t_x = (n_x \sigma_{xx} + n_y \sigma_{xy})$ and $t_y = (n_x \sigma_{xy} + n_y \sigma_{yy})$.

Previous system of equations needs to be written in matrix form. In case of small deformations for plane strain problem (thick body) in 2D [10], the stress-strain relation is $\sigma = C\varepsilon$ or

$$
\begin{Bmatrix} \sigma_{xx} \\ \sigma_{yy} \\ \sigma_{xy} \end{Bmatrix} = \begin{bmatrix} c_{11} & c_{12} & 0 \\ c_{21} & c_{22} & 0 \\ 0 & 0 & c_{66} \end{bmatrix} \begin{Bmatrix} \varepsilon_{xx} \\ \varepsilon_{yy} \\ 2\varepsilon_{xy} \end{Bmatrix},
\tag{19}
$$

and coefficients c_{ij} are for plane strain constitutive equation as follows:

$$
c_{11} = \frac{E_1(1 - \nu_{12})}{(1 + \nu_{12})(1 - \nu_{12} - \nu 21)}, \qquad \text{where} \quad \nu_{21} = \nu_{12} \frac{E_2}{E_1}
\tag{20}
$$

$$
c_{22} = \frac{E_2(1 - \nu_{21})}{(1 + \nu_{21})(1 - \nu_{12} - \nu 21)},
\tag{21}
$$

$$
c_{12} = \nu_{12} c_{22} \quad \text{and} \quad c_{66} = G_{12}.
\tag{22}
$$

Here the deformation ε can be found by using the matrix of derivatives

$$
D = \begin{bmatrix} \partial/\partial x & 0 \\ 0 & \partial/\partial y \\ \partial/\partial y & \partial/\partial x \end{bmatrix},
\tag{23}
$$

as $\varepsilon = Du$ where the displacements $u = [u_x \quad u_y]^T$ so

$$
\begin{Bmatrix} \varepsilon_{xx} \\ \varepsilon_{yy} \\ 2\varepsilon_{xy} \end{Bmatrix} = \begin{bmatrix} \partial/\partial x & 0 \\ 0 & \partial/\partial y \\ \partial/\partial y & \partial/\partial x \end{bmatrix} \begin{bmatrix} u_x \\ u_y \end{bmatrix} = \begin{bmatrix} \partial u_x/\partial x \\ \partial u_y/\partial y \\ \partial u_x/\partial y + \partial u_y/\partial x \end{bmatrix}.
\tag{24}
$$

Therefore the stresses are given through displacements in matrix format as

$$
\sigma = CDu.
\tag{25}
$$

Equations (18) can therefore be written as

$$
\int_\Omega \left\{ \begin{bmatrix} \partial/\partial x & 0 \\ 0 & \partial/\partial y \\ \partial/\partial y & \partial/\partial x \end{bmatrix} \begin{Bmatrix} w_1 \\ w_2 \end{Bmatrix} \right\}^T \begin{bmatrix} c_{11} & c_{12} & 0 \\ c_{21} & c_{22} & 0 \\ 0 & 0 & c_{66} \end{bmatrix} \begin{bmatrix} \partial/\partial x & 0 \\ 0 & \partial/\partial y \\ \partial/\partial y & \partial/\partial x \end{bmatrix} \begin{Bmatrix} u_1 \\ u_2 \end{Bmatrix} dx dy +
$$

$$
+ \int_\Omega \rho \begin{Bmatrix} w_1 \\ w_2 \end{Bmatrix}^T \begin{Bmatrix} \ddot{u}_x \\ \ddot{u}_y \end{Bmatrix} dx dy = \int_\Omega \begin{Bmatrix} w_1 \\ w_2 \end{Bmatrix}^T \begin{Bmatrix} b_x \\ b_y \end{Bmatrix} dx dy + \int_\Gamma \begin{Bmatrix} w_1 \\ w_2 \end{Bmatrix}^T \begin{Bmatrix} t_x \\ t_y \end{Bmatrix} ds,
\tag{26}
$$

11

which are in compact form, by using $(AB)^T = B^T A^T$

$$0 = \int_\Omega w^T D^T C D u \, dx dy + \int_\Omega \rho w^T \ddot{u} \, dx dy - \int_\Omega w^T b \, dx dy - \int_\Gamma w^T f \, ds. \qquad (27)$$

The variables u and $\ddot{u}$ are interpolated by shape functions

$$u_x \approx \sum_i \psi_i(x,y) u_x^i, \qquad u_y \approx \sum_i \psi_i(x,y) u_y^i. \qquad (28)$$

The same interpolation functions are used for weight functions w_i. This allows to extract the shape function constants u_x^i and u_y^i from the integration, leaving to integrate only predetermined functions ψ_i. Using three-node linear triangle element T3 with 2 degrees of freedom per node then the shape functions and constants can be expressed as (and will be defined later on)

$$\Psi = \begin{bmatrix} \psi_1, 0, \psi_2, 0, \psi_3, 0 \\ 0, \psi_1, 0, \psi_2, 0, \psi_3 \end{bmatrix}, \qquad (29)$$

and

$$\Delta = \{u_x^1, u_y^1, u_x^2, u_y^2, u_x^3, u_y^3\}^T, \qquad (30)$$

so the displacements and accelerations are

$$\begin{Bmatrix} u_x \\ u_y \end{Bmatrix} \approx \Psi \Delta \quad \text{and} \quad \begin{Bmatrix} \ddot{u}_x \\ \ddot{u}_y \end{Bmatrix} \approx \Psi \ddot{\Delta}. \qquad (31)$$

These can be substituted into Eqs. (27) and also w_1 and w_2 substituted by shape function ψ, since the equations must hold for every admissible weight function w.

Defining $B = D\Psi$, we can use

$$\varepsilon = Du = D\Psi\Delta = B\Delta \quad \text{and} \quad \sigma = CB\Delta, \qquad (32)$$

to express Eq. (27) as

$$0 = \int_\Omega \left(B^T C B \Delta \right) dx dy + \int_\Omega \rho \Psi^T \Psi \ddot{\Delta} \, dx dy - \int_\Omega \Psi^T b \, dx dy - \int_\Gamma \Psi^T f \, ds, \qquad (33)$$

where the constants Δ and $\ddot{\Delta}$ can be taken out of the integration. Here we used the fact that

$$B = D\Psi = \begin{bmatrix} \frac{\partial \psi_1}{\partial x} & 0 & \frac{\partial \psi_2}{\partial x} & 0 & \frac{\partial \psi_3}{\partial x} & 0 \\ 0 & \frac{\partial \psi_1}{\partial y} & 0 & \frac{\partial \psi_2}{\partial y} & 0 & \frac{\partial \psi_3}{\partial y} \\ \frac{\partial \psi_1}{\partial y} & \frac{\partial \psi_1}{\partial x} & \frac{\partial \psi_2}{\partial y} & \frac{\partial \psi_2}{\partial x} & \frac{\partial \psi_3}{\partial y} & \frac{\partial \psi_3}{\partial x} \end{bmatrix}, \qquad (34)$$

which is also $B = Dw$.

4.1 Matrix formulation of the Finite Element problem

Equation (33) can be expressed in matrix form as

$$M\ddot{\Delta} + K\Delta = F, \qquad (35)$$

where M is mass matrix, K is stiffness matrix, Δ is displacement vector and F is the force vector. This dynamical system can be solved by various methods which are explored in the next subsection.
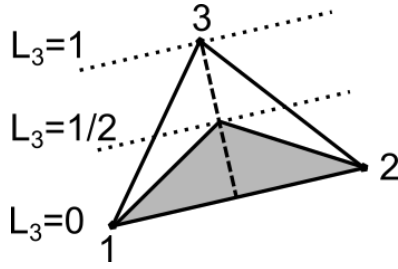
Figure 8: T3 element node numbering direction with shaded area describing area coordinate $L_3 = 1/2$

Regarding the body forces $b = 0$, the element matrices can be found as follows

$$M_e = \int_\Omega \rho \Psi^T \Psi dx dy, \tag{36}$$

$$K_e = \int_\Omega B^T C B dx dy, \tag{37}$$

$$F = \int_\Gamma \Psi^T f ds. \tag{38}$$

Equation (35) can be extended to include damping

$$M\ddot{\Delta} + C\dot{\Delta} + K\Delta = F, \tag{39}$$

which in this work used to apply the absorbing boundary conditions. Here C is the damping matrix. The Lysmer-Kuhlemeyer absorbing boundary conditions [12] give matrix C as diagonal matrix, which enables to take advantage of the explicit solvers. The computation of the diagonal matrix C from Lysmer-Kuhlemeyer boundary conditions is explained in Section 4.6.

4.2 Shape functions

Linear triangular elements T3 (Fig. 8), also known as constant strain triangle [10], were chosen for this problem for the following reasons. Firstly because the epoxy layers in the laminate model can be very small, therefore small elements are needed anyway, with T3 being computationally cheapest. Secondly linear elements are well suited for nonlinear problems: since the strain is constant throughout the element, the computation of nonlinear constitutive relations would also be simple. In this work the material itself is linear but future simulations might include nonlinearity or hysteresis.

The derivation of the mass matrix is a bit more involved than the stiffness matrix, because the shape functions (as opposed to their derivatives) are not elementwise constant. It involves determining it by using interpolation functions and then integrating using the numerical integration techniques. The integration could alternatively be done exactly, since $\rho = $ const and element is linear, but numerical integration is a more general method.

The interpolation functions can be written as

$$u_x \approx \sum_{j=1}^3 u_x^j \psi_j(\xi, \eta), \qquad u_y \approx \sum_{j=1}^3 u_y^j \psi_j(\xi, \eta). \tag{40}$$

For the T3 element, the shape functions can be found from a master element which is a right angled triangle in coordinate system ξ, η as shown in Fig. 9. This master is given in the "natural

13

coordinates" of the element ξ and η, and is used for numerically integrating over the element. The coordinates L_i for the triangle are the area coordinates which also coincide with the shape functions ψ_i [10]. For example, L_3 describes the area (shaded in Fig. 8) which is formed when the opposite side of node 3 is moved toward the node. If the line is moved to half way, then the area (shaded) is half of the total area of triangle and $L_3 = 1/2$.
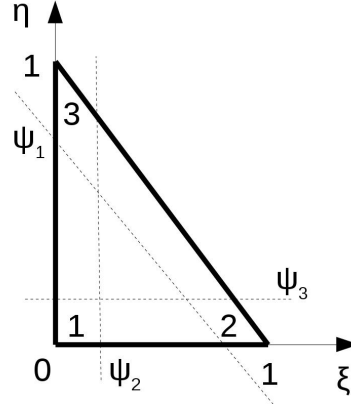

Figure 9: Master right triangle in element coordinate system (ξ, η)

The coordinates $L_i = \psi_i$ are the area coordinates and also the shape functions dependent on the master triangle coordinates ξ and η

$$L_1 = \psi_1 = 1 - \xi - \eta, \qquad L_2 = \psi_2 = \xi, \qquad L_3 = \psi_3 = \eta. \tag{41}$$

Since there are only two independent coordinates (ξ, η), the same applies for $L_i = \psi_i$: by specifying two of them, the third is implicitly given.

From Eqs. (40) and (41)

$$x = x_1(1 - \xi - \eta) + x_2\xi + x_3\eta, \tag{42}$$

$$y = y_1(1 - \xi - \eta) + y_2\xi + y_3\eta. \tag{43}$$

Inverting these for coordinates ξ and η dependent on the coordinates of the points of the triangle

$$\xi = \frac{1}{2A}\left[(x - x_1)(y_3 - y_1) - (y - y_1)(x_3 - x_1)\right], \tag{44}$$

$$\eta = \frac{1}{2A}\left[(y - y_1)(x_2 - x_1) - (x - x_1)(y_2 - y_1)\right], \tag{45}$$

where A is the area of the triangle. It is simple to find the derivatives of these shape functions by variables ξ and η, but in our formulas, we need derivatives $\frac{\partial \psi_i}{\partial x}$ and $\frac{\partial \psi_i}{\partial y}$. Using the chain rule in matrix notation we have

$$\left\{ \begin{array}{c} \frac{\partial \psi_i}{\partial \xi} \\ \frac{\partial \psi_i}{\partial \eta} \end{array} \right\} = \begin{bmatrix} \frac{\partial x}{\partial \xi} & \frac{\partial y}{\partial \xi} \\ \frac{\partial x}{\partial \eta} & \frac{\partial y}{\partial \eta} \end{bmatrix} \left\{ \begin{array}{c} \frac{\partial \psi_i}{\partial x} \\ \frac{\partial \psi_i}{\partial y} \end{array} \right\} = [J] \left\{ \begin{array}{c} \frac{\partial \psi_i}{\partial x} \\ \frac{\partial \psi_i}{\partial y} \end{array} \right\}, \tag{46}$$

where the Jacobian matrix $[J]$ describes the transformation

$$[J] = \begin{bmatrix} \frac{\partial x}{\partial \xi} & \frac{\partial y}{\partial \xi} \\ \frac{\partial x}{\partial \eta} & \frac{\partial y}{\partial \eta} \end{bmatrix}. \tag{47}$$

Table 2: Weights for integrating over the T3 element

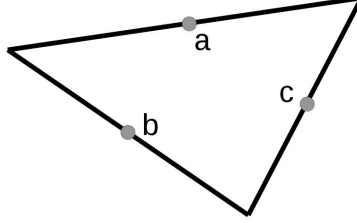| Point	$L_1 = \psi_1$	$L_2 = \psi_2$	$L_3 = \psi_3$	Weight W_I
a	1/2	0	1/2	1/3
b	1/2	1/2	0	1/3
c	0	1/2	1/2	1/3

Figure 10: Integration points on the T3 element

A Jacobian matrix can be used for the needed transformation from the real element to the master element. This is needed because it is much simpler to numerically integrate over the undeformed master element.

Using Eqs. (42) and (42), the Jacobian matrix is

$$[J] = \begin{bmatrix} x_2 - x_1 & y_2 - y_1 \\ x_3 - x_1 & y_3 - y_1 \end{bmatrix} = \begin{bmatrix} \gamma_3 & -\beta_3 \\ -\gamma_2 & \beta_2 \end{bmatrix}, \tag{48}$$

where coefficients are in often-used notation

$$\begin{aligned} \beta_1 &= y_2 - y_3, & \gamma_1 &= x_3 - x_2, \\ \beta_2 &= y_3 - y_1, & \gamma_2 &= x_1 - x_3, \\ \beta_3 &= y_1 - y_2, & \gamma_3 &= x_2 - x_1, \end{aligned} \tag{49}$$

so the Jacobian determinant is $|J| = (x_2 - x_1)(y_3 - y_1) - (y_2 - y_1)(x_3 - x_1) = \beta_2\gamma_3 - \gamma_2\beta_3 = 2A$.

4.3   Numerical integration

As mentioned, the master element with shape functions ψ_i is used for the numerical integration. After transforming integrals from (x, y) coordinate system to (ξ, η) system, the master triangular T3 element enables numerical integration by only evaluating the field at three points of the triangle.

$$\int_\Omega F(x, y) dx dy = \int_\Omega F(\xi, \eta) |J| d\xi d\eta \approx \sum_{I=1}^{3} W_I F(\xi, \eta) |J| \tag{50}$$

These integration points are shown in Fig. 10, their coordinates and weights in Table 2. Here ψ_1 is linearly dependent on $\psi_2 = \xi$ and $\psi_3 = \eta$ (the two independent variables).

4.4   Element mass matrix

The consistent mass matrix for the T3 element can be generated from Eq. (36) by using the shape functions to integrate over the element, supposing that the material inside the element

is homogeneous ($\rho = const.$). The elements of the element mass matrix are given by

$$M_{ij} = \int_\Omega \rho \psi_i \psi_j dx dy = \rho \int_\Omega \psi_i \psi_j |J| dL_2 dL_3 = 2A\rho \int_\Omega \psi_i \psi_j dL_2 dL_3$$
$$\approx A\rho \sum_{I=1}^3 \frac{1}{3} \psi_i(S_I)\psi_j(S_I), \tag{51}$$

where $|J| = 2A$ is the Jacobian determinant and S_I are the quadrature locations, yielding relations for mass entries in the element matrix as

$$M_{11} = A\rho \frac{2}{12}, \tag{52}$$

$$M_{12} = M_{13} = M_{23} = A\rho \frac{1}{12}. \tag{53}$$

Naturally, the mass matrix is symmetrical, so if there are 2 degrees of freedom per node then element mass matrix becomes

$$M_e = \frac{\rho A}{12} \begin{bmatrix} 2 & 0 & 1 & 0 & 1 & 0 \\ & 2 & 0 & 1 & 0 & 1 \\ & & 2 & 0 & 1 & 0 \\ & & & 2 & 0 & 1 \\ & & & & 2 & 0 \\ & & & & & 2 \end{bmatrix}. \tag{54}$$

4.5 Element stiffness matrix

The shape functions of the T3 element can be expressed from Eqs. (41), (42) and (43) as

$$\psi_i = \frac{1}{2A}(\alpha_i + \beta_i x + \gamma_i y), \tag{55}$$

and their derivatives are

$$\frac{\partial \psi_i}{\partial x} = \frac{\beta_i}{2A} \quad \text{and} \quad \frac{\partial \psi_i}{\partial y} = \frac{\gamma_i}{2A}, \tag{56}$$

which are used to calculate the matrix B from Eq. (34)

$$B = \frac{1}{2A} \begin{bmatrix} \beta_1 & 0 & \beta_2 & 0 & \beta_3 & 0 \\ 0 & \gamma_1 & 0 & \gamma_2 & 0 & \gamma_3 \\ \gamma_1 & \beta_1 & \gamma_2 & \beta_2 & \gamma_3 & \beta_3 \end{bmatrix}, \tag{57}$$

Since this is a constant strain triangle, integrating the element stiffness matrix is simple: constant value of strain dependent stiffness times the area. Equation (57) can be used to find the stiffness matrix of a single element, knowing its elasticity matrix C and dimensions, by

$$K_e = A_e B_e^T C_e B_e, \tag{58}$$

which is the element stiffness matrix.

4.6 Boundary conditions

Degrees of freedom are fixed by zeroing the appropriate degrees of freedom in the $(M \cdot C)^{-1}$ matrix. In this study, four degrees of freedom are fixed (Fig. 3).

Lysmer and Kuhlemeyer absorbing boundary conditions [12] are used on the bottom and left edges of the simulation region. At the moment, the simplest boundary conditions are used where the wave velocity is averaged even for the left-hand boundary where the model is layered. The Lysmer-Kuhlemeyer absorbing boundary conditions are applied as viscous stresses on the boundaries, which means that they can be applied directly to DOF, making the damping matrix C diagonal. The viscous stresses that are applied to boundaries are [12]

$$c_{ii} = \int_{\Gamma} a\rho V_p ds, \quad \text{normal motion DOF,} \tag{59}$$

$$c_{ii} = \int_{\Gamma} b\rho V_s ds, \quad \text{shear motion DOF,} \tag{60}$$

where Γ is the boundary portion of the element. In this work the scaling parameters are $a = 1$ and $b = 1$. The wave velocities used by these boundary conditions are [13]

- $V_p = 2972$ m/s,

- $V_s = 1956$ m/s.

4.7 Global matrix assembly

The external force vectors are not integrated using the shape functions. The force on line elements is simply divided between the nodes of the line.

Since each node has two degrees of freedom, then the global mass and stiffness matrices are with dimension $2n \times 2n$ where n is the number of nodes. For each degree of freedom of node, the values from the element matrices are mapped to the global matrices as in the usual way described in the literature [10, 14]. There are several lumping schemes available for mass matrices [14]. In this work, the rows are summed into the diagonal element.

The resulting Eq. (39) can be solved by various timestepping methods.

4.8 Time stepping algorithms

The main problem (Eq. (39)) is solved using a hand-coded solver with central difference time stepping. The verification of the time-stepping method was done using implicit Newmark method and the solver was verified by running the non-contact problem in parallel with solution using FEniCS.

4.8.1 Newmark algorithm

With Newmark's method, the timestep was ($\Delta t_{\mathrm{s}} = 5 \cdot 10^{-8}$ s). The constant average acceleration Newmark's scheme has following relations

$$\begin{cases} \dot{u}_{s+1} = \dot{u}_s + \Delta t_{\mathrm{s}} \frac{\ddot{u}_s + \ddot{u}_{s+1}}{2}, \\ u_{s+1} = u_s + \Delta t_{\mathrm{s}} \dot{u}_s + (\Delta t_{\mathrm{s}})^2 \frac{\ddot{u}_s + \ddot{u}_{s+1}}{4}. \end{cases} \tag{61}$$

yielding a relation for acceleration

$$\ddot{u}_{s+1} = \frac{4}{(\Delta t)^2} (u_{s+1} - u_s) - \frac{4}{\Delta t} \dot{u}_s - \ddot{u}_s \tag{62}$$

which is substituted into the variational Eq. (13)

$$\int_\Omega \left(\rho \frac{4}{(\Delta t)^2} u_{s+1} \right) \cdot \delta u \, dxdy + \int_\Omega \sigma_{ij} \cdot \delta \varepsilon_{ij} dxdy \tag{63}$$

$$= \int_\Omega \rho \left(\frac{4}{(\Delta t)^2} u_s + \frac{4}{\Delta t} \dot{u}_s + \ddot{u}_s \right) \cdot \delta u \, dxdy + \int_\Gamma f \cdot \delta u \, ds. \tag{64}$$

More details on the application of the Newmark's scheme for solving Eq. (39) can be found from Reddy [10] or Zienkiewicz [14].

4.8.2 Central difference algorithm

The main advantage of the central difference algorithm over the Newmark is that it is explicit and therefore by using lumped mass matrix gives better performance in case of small timesteps (here $\Delta t = 5 \cdot 10^{-10}$ s). Small timesteps are advantageous in case of contact problems, since the problem can become indeterminate as to when the contact conditions are satisfied and the friction contact needs to be computed. There is much ongoing work in how to calculate the contact conditions in these elastodynamic cases [15, 16, 17]. The contact condition used in this work is described in Section 4.9.

If the mass matrix is diagonal (so instead of mass spread out evenly throughout the material, it is "lumped" into the nodes), then the solution of the problem becomes a multiplication with an inverse of a diagonal matrix, which is trivial. Using the central difference algorithm on the Eq. (35) with timestep Δt, we arrive at

$$\left(\frac{M}{\Delta t^2} + \frac{C}{2\Delta t} \right) u_{n+1} = F_n - \left(K - \frac{2M}{\Delta t^2} \right) u_n - \left(\frac{M}{\Delta t^2} - \frac{C}{2\Delta t} \right) u_{n-1}. \tag{65}$$

This explicit scheme is solved by dividing the equation by the term in the first parentheses, which is simple to do if M and C are lumped (vectors instead of big, sparse matrices). In linear material, additional simplifications come from the stiffness matrix K being constant. Therefore the solution for each new timestep can be expressed as

$$u_{n+1} = D \cdot (F_n - A \cdot u_n - B \cdot u_{n-1}), \tag{66}$$

where we have precomputed

$$A = K - \frac{2M}{\Delta t}, \tag{67}$$

$$B = \frac{M}{\Delta t^2} - \frac{C}{2\Delta t}, \tag{68}$$

$$D = \left(\frac{M}{\Delta t^2} + \frac{C}{2\Delta t} \right)^{-1}. \tag{69}$$

The speed advantage of this explicit method comes from the fact that D is easy to invert if it is a diagonal matrix. Then the solution u_{n+1} can be found by just a vector-vector or matrix-vector multiplication.

4.9 Contact gap modelling

There is a single source of nonlinearity in this simulation: the contacting crack fully inside the material. If the material is at rest, then the crack is small and straight. In this work, there is neither a preload nor an initial gap in the contacting crack. This simple material defect results in a localised nonclassical nonlinearity, which can be analysed by various signal processing methods.

It is known that frictional contact problems can be sensitive to timestep length and loading path [18]. In this work, it is assumed that the small timestep length and relatively small forces involved keep the error small. Therefore an explicit solution method scheme is utilized, similar to [19]. A more precise solution could be expected from an implicit scheme [18], but that is left for the future. Further refinements could include thermoelastic contribution to the constitutive equation at the frictional contact gap [3].

The node-to-node contact model is used. This is the simplest method, as the displacements between the contacting surfaces can be computed easily. For this simulation, the nodes on the top surface of the crack is labelled "master" and the bottom "slave". In this work, the defect is horizontal, simplifying the calculation of normal gap between the nodes. With nodes labelled as in Fig. 11, the normal contact gap $g_N = n_y^s - n_y^m$ and the tangential gap (offset) is $g_T = n_x^s - n_x^m$. In case of normal penetration of one surface into another, then $g_N > 0$. If there is no penetration, then $g_N \leq 0$. The coefficient of friction is $\mu = 0.6$, and the solution aims to satisfy the Kuhn-Tucker conditions on the crack surface:

$$\begin{cases} g_N \leq 0, \\ \lambda_N = \sigma \cdot n \leq 0, \\ g_N \cdot \lambda_N = 0, \end{cases} \tag{70}$$

where λ_N is the normal force on crack, σ is stress and n is the normal vector of the surface. The penalty plus Lagrange multiplier method [20] is used for normal contact and the penalty method for friction.
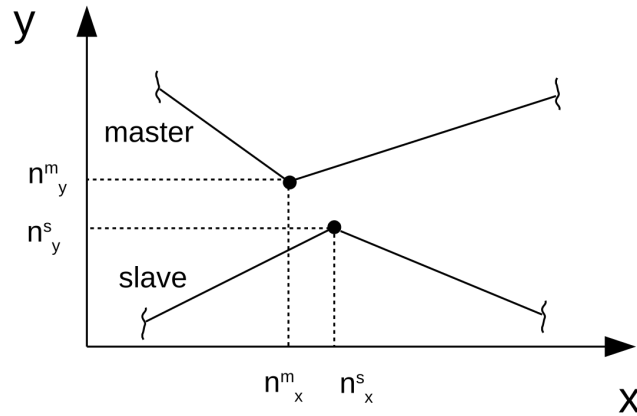

Figure 11: Contact gap node measurement scheme for a single node pair

Figure 12 shows the flowchart of the code logic with Coulomb friction. The steps are shown for one node-to-node contact and are applied to each node pair in contact where contact is detected.

The different treatment paths of different nodes can be concluded as in the following steps.
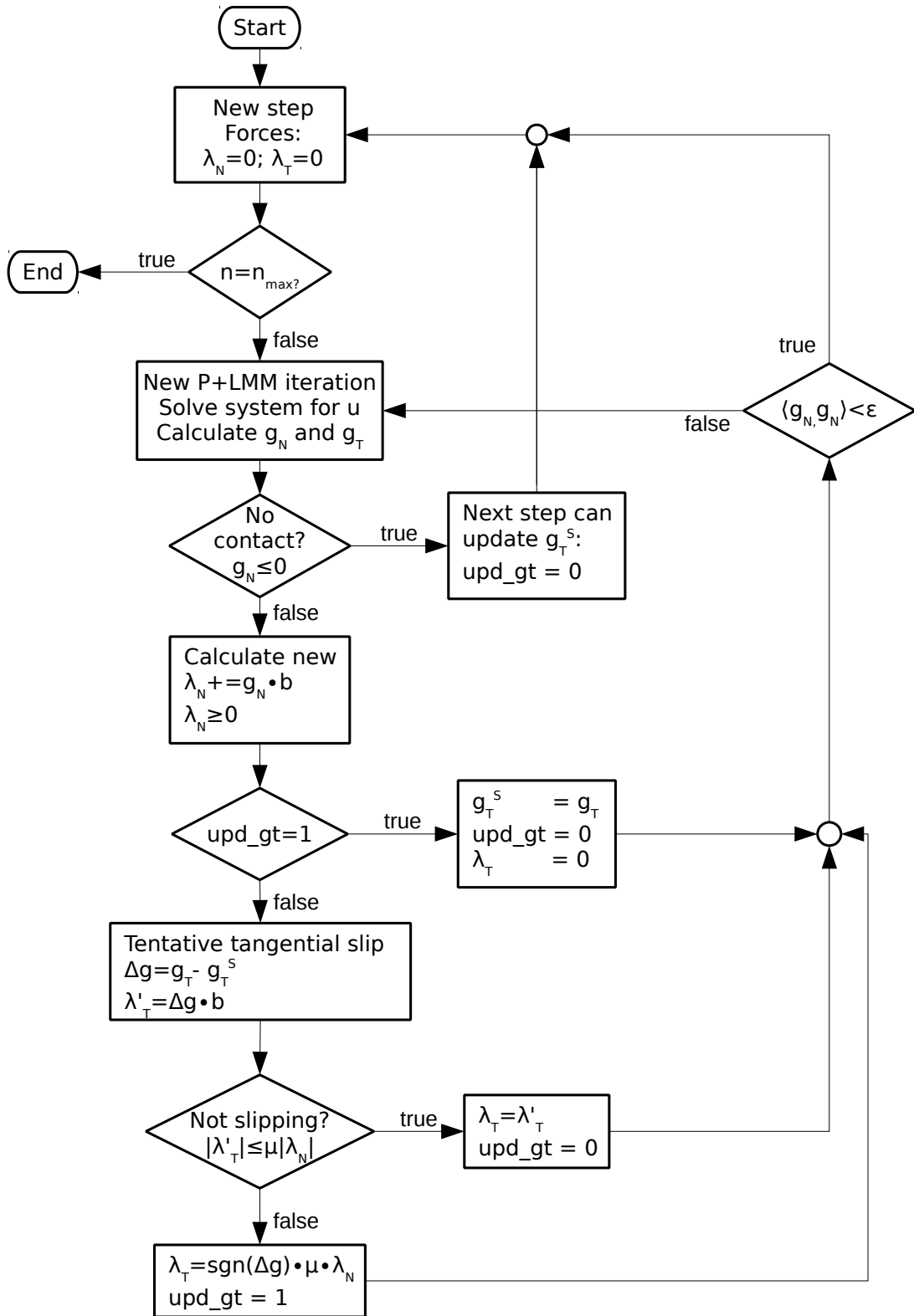
Figure 12: Logic of the contact gap code

- The initial contact forces are zeroed: $\lambda_N = 0$, $\lambda_T = 0$.

- System is solved: $(M/\Delta t^2 + C/2\Delta t)\, u^{n+1} = F^n - (K - 2M/\Delta t^2)\, u^n - (M/\Delta t^2 - C/2\Delta t)\, u^{n-1}$.

- Vector gap functions are found: $g_N = n_y^s - n_y^m$ and $g_T = n_x^s - n_x^m$.

- Normal forcing updated $\lambda_N = \lambda_N + g_N b$ where b is some big penalty value and $\lambda_N \geq 0$.

- Logic diverges to 3 paths shown in Table 3.

- The normal contact condition is verified by setting the penetration value $g_P = g_N$ and $g_P \geq 0$. Then the L^2-norm is evaluated $\langle g_P | g_P \rangle < \varepsilon$ where ε is the limiting value for the error due to contact penetration. If the condition is not fulfilled, the iteration is repeated, otherwise new timestep is taken.

Table 3: Three possible logic paths for contact calculation

1)	2)	3)	
$g_N \leq 0$	$g_N > 0$ and upd_gt = True	$g_N > 0$ and upd_gt = True	
No contact	Either: a) first iteration with contact, or b) previous iteration had tangential slip	Previous iteration had non-slip frictional contact, we have valid saved g_T^s	
upd_gt = True $\lambda_T = 0$	upd_gt = False $g_T^s = g_T$ $\lambda_T = 0$		
		Tentative tangential slip $\Delta g = g_T - g_T^s$ $\lambda_T' = \Delta g b$	
		a) slipping if $\|\lambda_T'\| > \mu\|\lambda_N\|$: $\lambda_T = sgn(\Delta t)\mu\lambda_N$ upd_gt = True	b) sticking if $\|\lambda_T'\| \leq \mu\|\lambda_N\|$: $\lambda_T = \lambda_T'$ upd_gt = False

4.10   Error management

The programming errors are checked by comparison between different FEM simulation programs solving the same problem. The simplest error check is by comparison. Three cases are compared:

- hand-programmed FEM program with explicit central difference timestep,

- hand-programmed FEM program with implicit Newmark timestep,

- FEM program using FEniCS libraries [21] with implicit Newmark timestep.

Figure 13 shows the test case displacements in y-direction when the input has been a 30 μs long chirp signal. The purpose of the comparisons are twofold: firstly to confirm that the assembly of the matrices and timestepping is done correctly in the hand-programmed software and secondly to confirm that the explicit timestepping algorithm gives a good result in this problem. It is better to use explicit timestepping, since in conjunction with lumped mass matrix, it is possible to get fast execution times. Also it is important because small timestep helps solve the contact problem better by finding the time of contact more precisely.
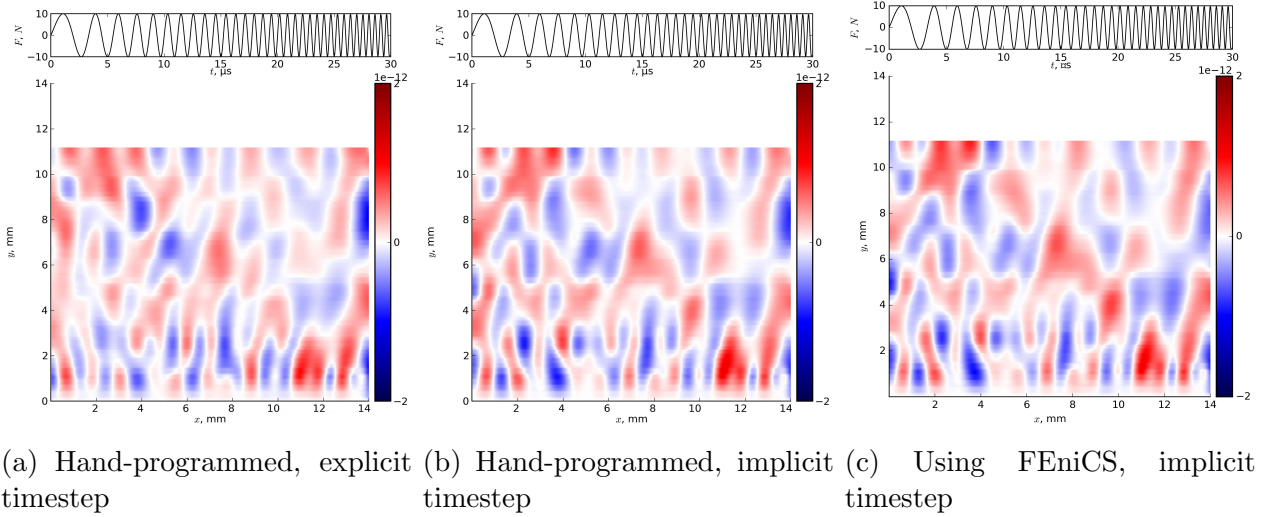

(a) Hand-programmed, explicit timestep (b) Hand-programmed, implicit timestep (c) Using FEniCS, implicit timestep

Figure 13: Comparison between solution programs and timesteps at the end of a 30 μs chirp signal

In verification simulations, the fixed Dirichlet boundary conditions are used at the bottom and left boundaries instead of absorbing boundary conditions. Later the linear problem with contact defects and absorbing boundary conditions is solved using only the hand-coded solver.

4.10.1 Energy conservation and dissipation

Errors in physical formulation can be checked using conservation laws. The wave energy is introduced at the transducer area. For the cracked part, we necessarily have dissipation. The energy also "exits" the through the absorbing boundaries. The total energy inside the boundaries plus the fluxes on the boundaries and dissipation on the defect should yield a constant value. This energy balance should indicate the quality of the simulation.

5 Simulation results and analysis

This section describes the signal analysis of the simulation results on the damaged and undamaged medium. The purpose is to list some analysis measures which could allow to detect the presence of damage as nonlinearity in materials when only a signal from a point source is available, like in ultrasonic NDT where transducer usually gives just a time-series of data, measured at one discrete point. The signals are low-pass filtered to keep only the ultrasonic component.

5.1 Input signal and simulation configuration

Equation (6) is used for the initial input signal of the TR-NEWS signal processing (Section. 3) into the simulation. It is a linear chirp with starting frequency $f_0 = 0.2$ MHz, ending frequency $f_1 = 2$ MHz and length of $t_1 = 30$ μs in the 60 μs long input signal,

$$c(t) = A \cdot \sin(\psi(t) \cdot t), \tag{71}$$

where

$$\psi(t) = 2\pi \left(f_0 \cdot t_1 + \frac{(f_1 - f_0) \cdot t^2}{2t_1} \right). \tag{72}$$

The resulting output of the simulation from this chirp then used according to the TR-NEWS signal processing to get the correlation data, which is time reveresed and resent through the simulation. The signal is applied at the Tx region (Fig. 14) as forcing with maximum amplitude of 50 kPa.
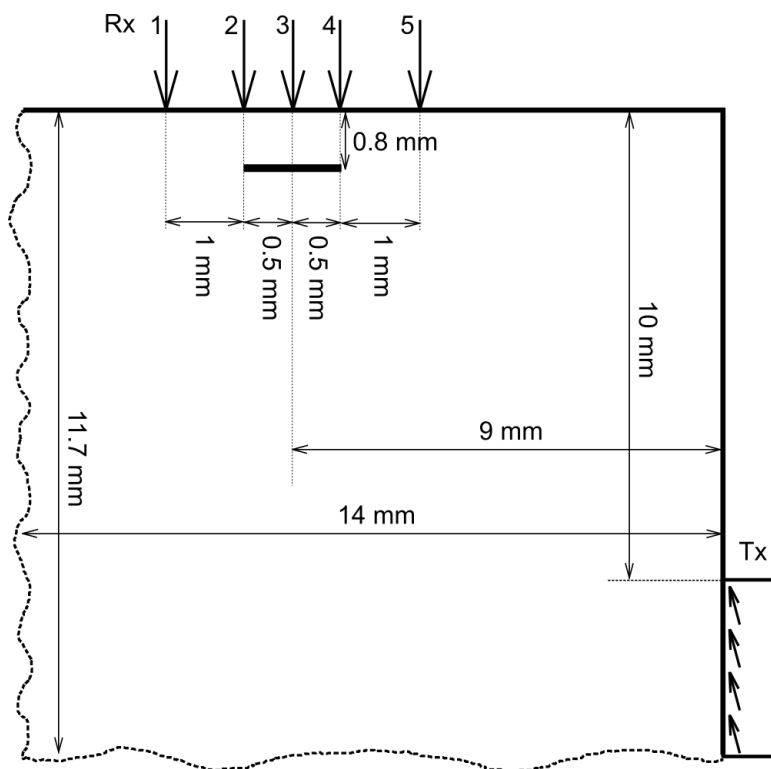

Figure 14: Sketch (not to scale) of the simulation geometry, location of crack, transmitter and receiver points without the layers

The input signal is transmitted at a 70° angle, the output signal is saved at five locations on the top of the simulation region (Fig. 14) marked from 1 to 5. Identical simulations are conducted on cracked and uncracked setup. Additionally the displacement field is saved as an image plot at each $5 \cdot 10^{-8}$ s (each 100 timesteps).

5.2 Undamaged CFRP TR-NEWS simulation

Figure 15 shows the TR-NEWS results of the uncracked CFRP test object simulation for the receiving transducer positions 1 to 5 (Fig. 14). It is an ordinary TR-NEWS focusing where at the middle of the signal there is the focusing, surrounded by the sidelobes. There are

two aspects to note about this is figure. Firstly, the sidelobes shift toward the main focusing and comparatively decrease in amplitude as the receiving transducer position shifts toward the transmitting transducer (from position 1 to position 5), indicating lower noise as the signal gets stronger. Secondly, the sidelobes are symmetrical in respect to the main lobe. This does not happen in nonlinear (damaged) material analysed later on. Additionally, PI signal processing was applied to this linear and uncracked material simulation which verified the nonexistence of nonlinearity (the results were identical).
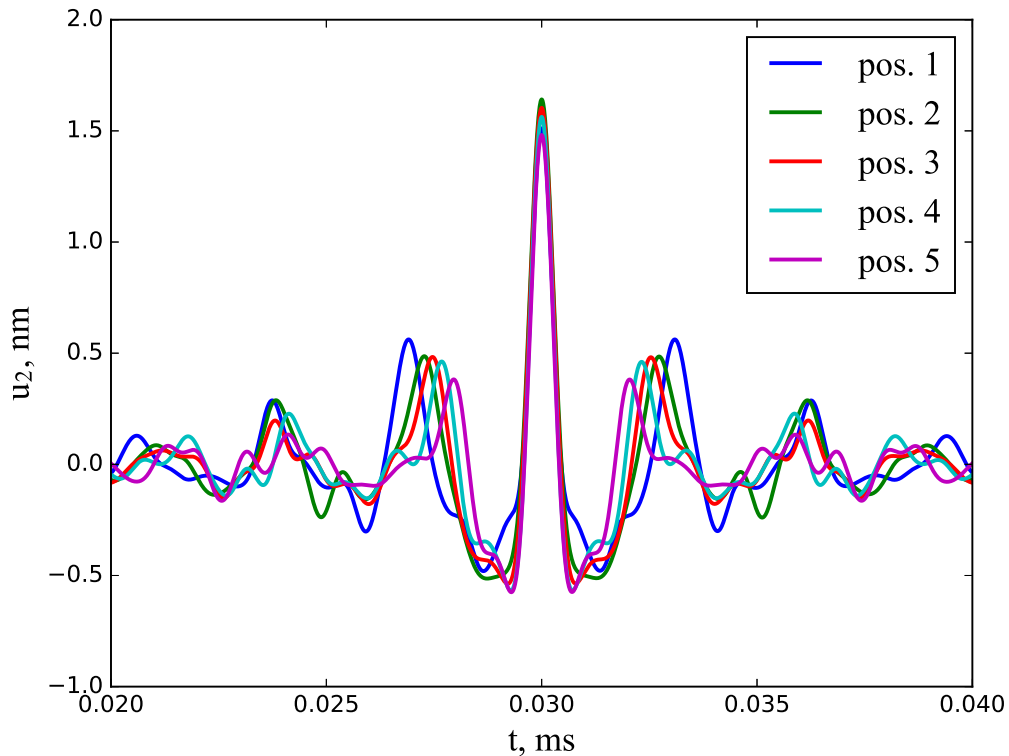

Figure 15: Unnormalized TR-NEWS focusing of undamaged CFRP simulation

5.3   Damaged CFRP TR-NEWS simulation

Figure 16 shows the TR-NEWS results of the cracked CFRP test object simulation for the receiving transducer positions 1 to 5 (Fig. 14). Here also the PI signal processing is applied and shows the nonlinearity as difference between 180° phase-shifted chirp signals, denoted as positive and negative excitation. It can be noted that the unlike the linear, uncracked case, the nonlinear, damaged case exhibits strong nonlinearity particularly strongly in receiving position 3 (middle of the crack). Additionally the sidelobes are unsymmetrical in respect to the main lobe. There is considerably more randomness in the side lobe signals across the measurement points. Figure 17 shows the envelope of this measure of nonlinearity across all of the measuring points. The nonlinearity magnitude depends on the measuring point location in respect to the crack: point 3 near the middle of the crack shows strongest nonlinearity, points 2 and 4 show less, and points 1 and 5 show the least.

Figure 18 shows the unnormalized focusing signal for the damaged medium, which can be compared with corresponding undamaged result in Fig. 15. The amplitudes of the focused signals have some interesting properties:
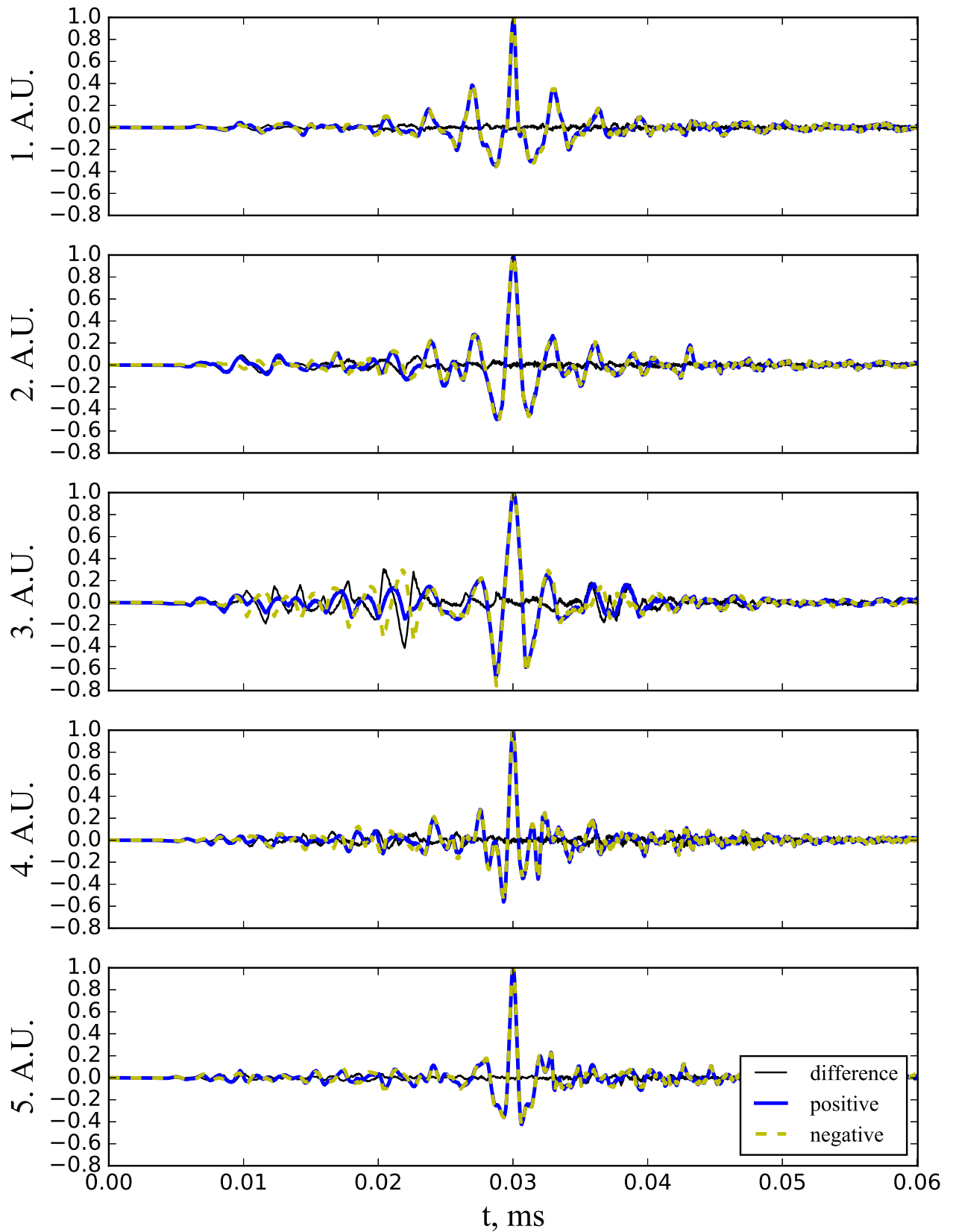
Figure 16: Normalized TR-NEWS focusing of damaged CFRP simulation with PI applied to detect nonlinearities as difference between negative and positive excitations

1. The highest amplitude comes not from the receiver position closest to the transmitter (pos. 5), but the one closest to the crack (pos. 3).

2. Comparing the amplitudes of the positions 2 and 4, at far side and near side of the crack end, respective to transmitter: the farther position has larger focusing amplitude than the nearer position. Since the simulation region has two absorbing boundaries, the wave propagation is mostly in one direction, therefore the defect between pos. 2 and 4 must be capturing the input signal and the correlation is using that energy as a new "virtual transducer" for the pos. 2 focusing in TR-NEWS signal processing. This could be further analysed in future works by the correlation signals which generate these focused signals, but is out of the scope for this paper.

3. Amplitudes of measurement positions 1 and 5 are "right way" around: the nearer measurement point has larger focusing amplitude than the farther.

Figure 19 shows a snapshot of the simulation u_2 displacement at a time moment $t = 32.6$ μs, just after the focusing. The defect in material is acting as a source of new excitation after TR-NEWS focusing. Wave energy is captured between the damage and outside wall of the material and emitted as a wave. Video of the displacement fields of a TR-NEWS focusing to point 3 of the damaged medium is available at [22].
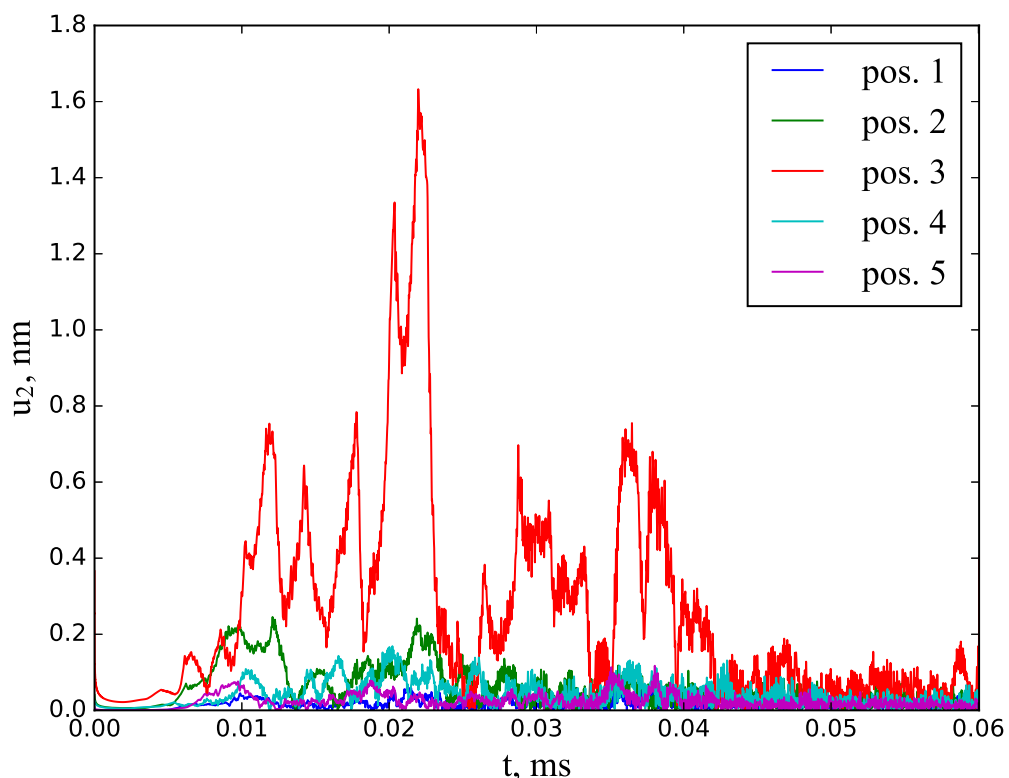

Figure 17: Envelopes of the PI nonlinearity measures from all of the measuring points

5.4   Spectral analysis of the focused signal

An often used indicator of nonlinear effects is the spectral analysis. While linear systems keep the frequency content constant, the nonlinear effects modify the frequencies which are present.
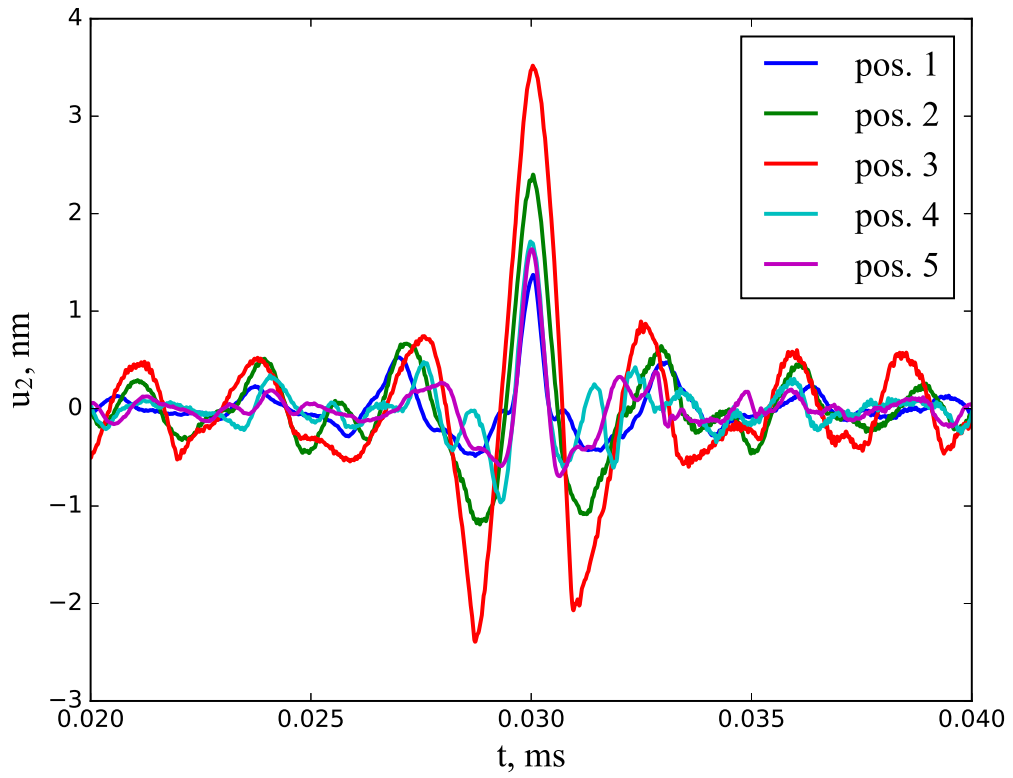
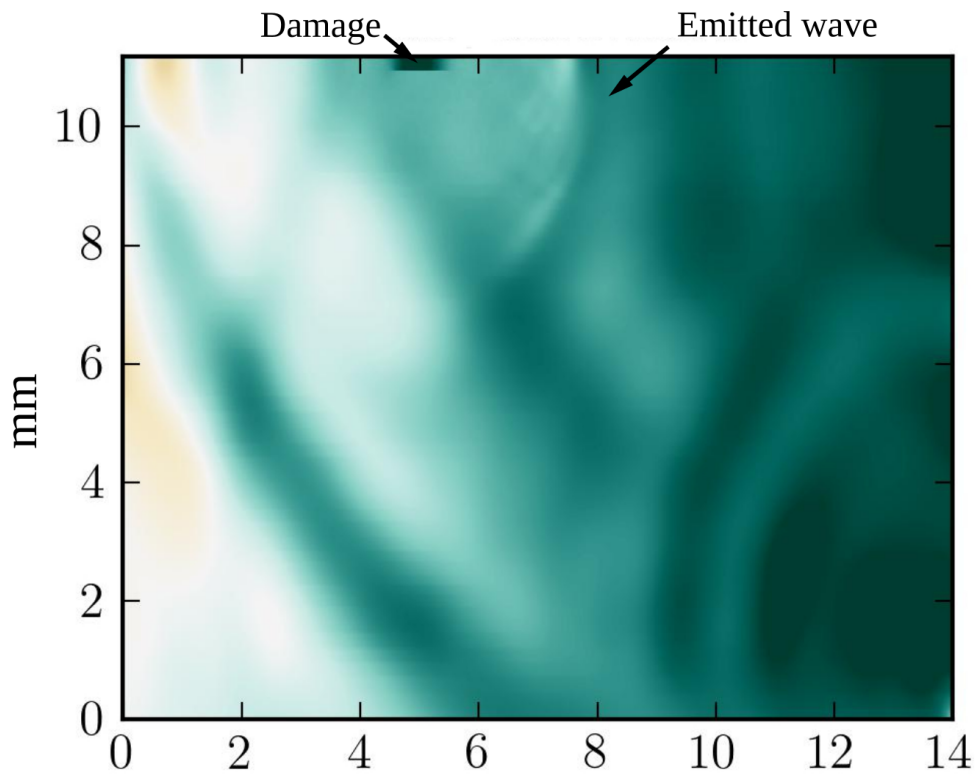Figure 18: Unnormalized TR-NEWS focusing of damaged CFRP simulation

Figure 19: Displacement u_2 field at time $t = 32.6$ μs with a wave emission coming from the damaged region. Video available at [22]

Figure 20 shows the spectral densities of the input chirp versus the output signals at point 3 of cracked and uncracked medium simulations. A definite difference in spectrum can be seen. The damaged medium exhibits more energy in the lower frequencies and less in higher frequencies, probably either due to defect resonance or the "mechanical diode" effect of the contacting nonlinearity which only allows one-sided passing of an impinging wave.

5.5 Spectral analysis of the defect motion

In addition to the data gathered at points 1 to 5 shown in Fig. 14, the simulations also saved the data at the crack itself (master and slave surface nodes). This allows to analyse, for example, the time series of the defect motion itself or compute the spectrum of the defect, shown in Fig. 21. This data is unavailable in physical ultrasonic NDT measurements, but in simulation allows to see what kind of spectrum does the defect generate and how the this translates to the measurement at point 3 on the surface near the defect. The interesting points in the spectrum of the defect are where it is larger than the undamaged medium signal on the surface and even better when it has visibly affected the spectrum of the on-surface measurement of the damaged medium. The four most prominent peaks in the spectrum of the defect are at 58, 116, 365 and 472 kHz.
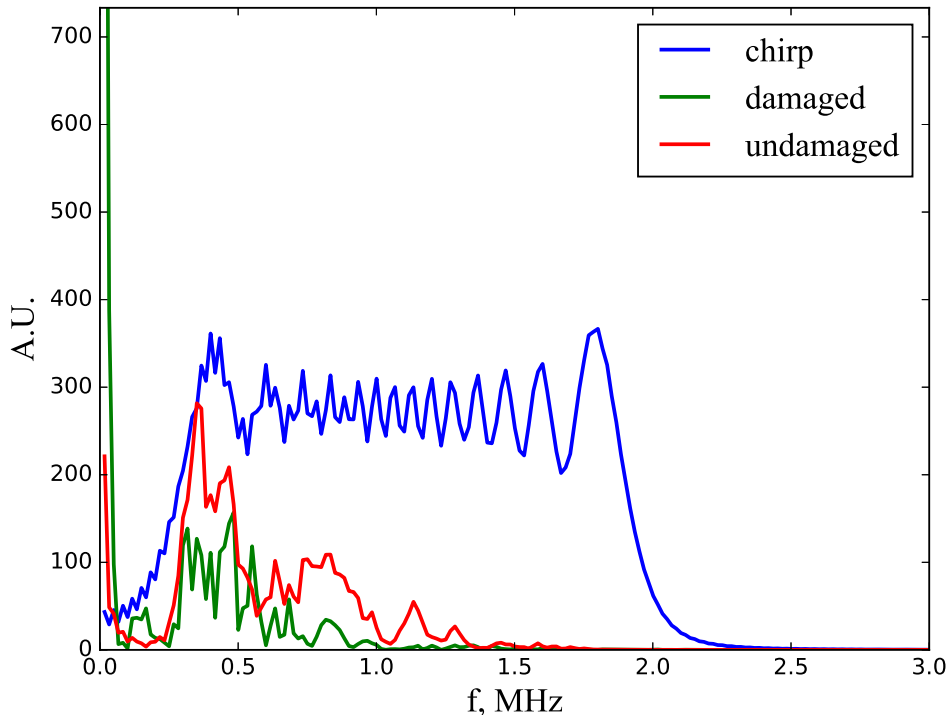

Figure 20: Spectral densities of input versus output signals of uncracked and cracked medium at point 3

5.6 Delayed TR-NEWS analysis

Section 3 describes also the delayed TR-NEWS signal processing method which allows to create arbitrary envelope wave at the focusing using Eq. (10), instead of the simple peak of the TR-NEWS. Equation (11) shows that in linear material the outcome of the delayed TR-NEWS process can be predicted. Since this method with prediction works very well in physical NDT
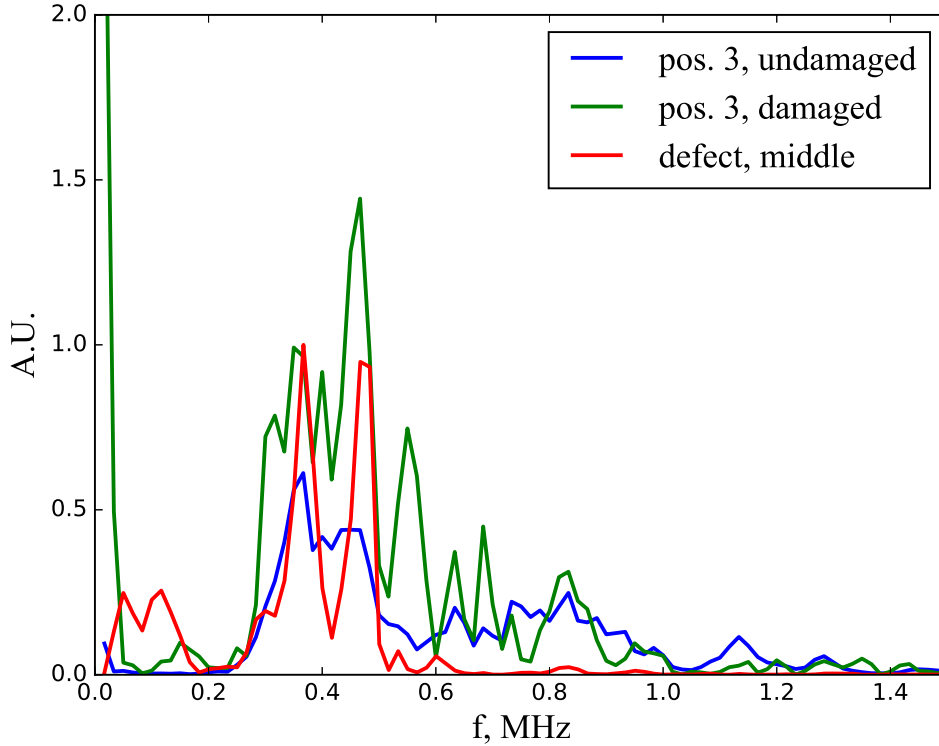
Figure 21: Spectral densities of the wave motion on the surface of the defect, compared to the nearest measurement point position 3 (damaged and undamaged)

measurements [8], it has been tested now in simulation with the nonlinearity, supposing that any difference from the prediction shows the presence of nonlinearities or damage. Figure 22 shows the comparison between the linear superposition prediction and the simulation result of a simple delayed TR-NEWS process where two focusing peaks are at superposition with 1 μs time delay. The difference between the prediction and the simulation are large and obvious, indicating the presence of nonlinearity. This measure of nonlinearity seems to be stronger than the measure calculated from PI (Fig. 16).

The delayed TR-NEWS signal processing could also be used in simulation according to the resonant frequency of the contacting gap, to try and excite the crack with even more wave energy, but this is out of the scope of the current paper.

6 Conclusion

The purpose of this research report was to list in detail the simulation methods and main results for the analysis of a defect inside a CFRP block. It describes the FEM simulations of a damaged medium, which are conducted to simulate the physical measurements of a damaged CFRP block using TR-NEWS ultrasonic signal processing. The mathematical and FEM models are described, the TR-NEWS signal processing is explained for attaining the simulation results. The results are shown for identical damaged and undamaged model, listing the differences using various signal processing methods, like PI, spectral analysis and delayed TR-NEWS to detect the presence of the damage as nonlinearity.

The simulation of the nonlinearity as one small crack near the receiving transducer allows to investigate more closely the mechanics of the contacting damage. It is sufficiently simple
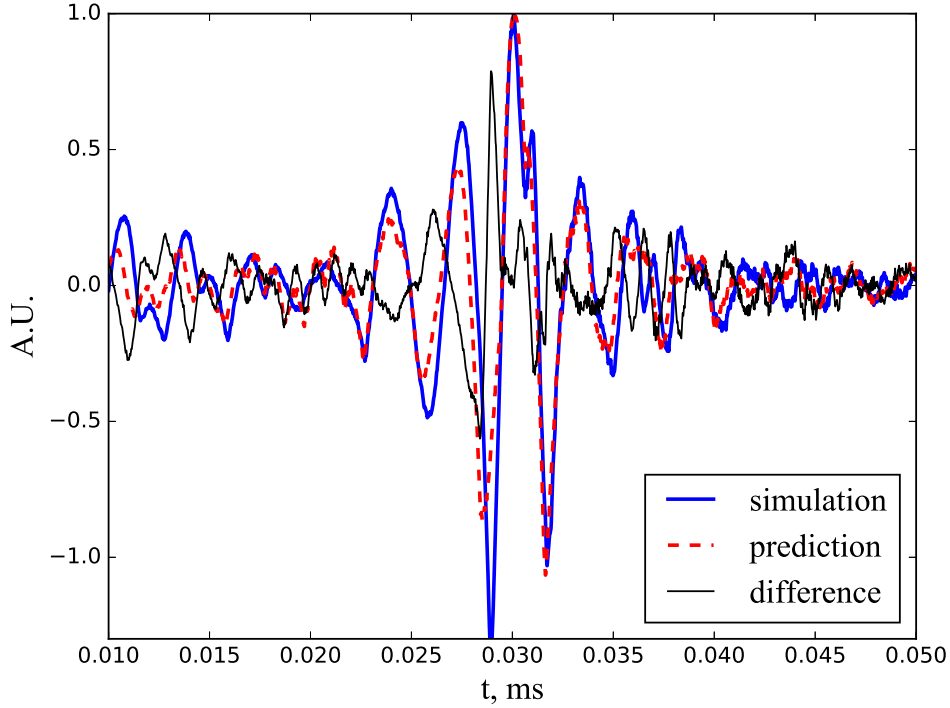
Figure 22: Delayed TR-NEWS signal processing with one delay of amplitude $a_i = 1$ and delay value $\tau = 1\,\mu$s (Eq. (11)): comparison between the linear prediction and the simulation outcome

model to use for developing new signal processing methods to extract the nonlinear signature of the material. It has been shown that the defect acts as an energy pocket, which can lead to development of a global method to detect defects farther away from the receiving transducer.

6.1 Perspectives

A more thorough investigation is possible using a combination of the signal processing methods shown. Also, a number of smaller ideas for detecting and analysing the damage in the material have been listed in this work which are out of the scope, but could be investigated in the future.

- Delayed TR-NEWS could be used in simulations to activate the defect by its resonance frequency.

- The symmetry breaking of sidelobes by the defect could be analysed, as the undamaged material has symmetric sidelobes.

- An automatic mesh refinement could be used to study the crack propagation for this kind of computational model.

- A 2D model consisting of elliptical yarns could be devised which keeps the complexity lower than the laminate model if the epoxy inclusions could be controlled to be large enough for larger elements.

- The simulation model could be made more complex and precise, for example by including thermodynamic frictional heating of the contact.

References

[1] I. Y. Solodov, N. Krohn, G. Busse, CAN: an example of nonclassical acoustic nonlinearity in solids, Ultrasonics 40 (1) (2002) 621–625.

[2] V. Aleshin, K. Van Den Abeele, Micro-potential model for acoustical hysteresis, in: Proceedings of the 18th International Congress on Acoustics, Vol. 3, 2004, pp. 1859–1862.

[3] I. Y. Solodov, B. A. Korshak, Instability, Chaos, and "Memory" in Acoustic-Wave – Crack Interaction, Phys. Rev. Lett. 88 (1).

[4] I. Y. Solodov, N. Krohn, G. Busse, Nonlinear ultrasonic NDT for early defect recognition and imaging, in: Proceedings of European conf. on NDT (ECNDT), 2010, pp. 734–758.

[5] S. Dos Santos, Z. Prevorovsky, Imaging of human tooth using ultrasound based chirp-coded nonlinear time reversal acoustics, Ultrasonics 51 (6) (2011) 667–674.

[6] J. Riviere, S. Haupert, P. Laugier, T. Ulrich, P.-Y. Le Bas, P. A. Johnson, Time reversed elastic nonlinearity diagnostic applied to mock osseointegration monitoring applying two experimental models, The Journal of the Acoustical Society of America 131 (3) (2012) 1922–1927.

[7] S. Dos Santos, C. Plag, Excitation symmetry analysis method (ESAM) for calculation of higher order non-linearities, Int. J. Nonlinear. Mech. 43 (2008) 164 – 169.

[8] M. Lints, S. Dos Santos, A. Salupere, Solitary waves for Non-Destructive Testing applications: Delayed nonlinear time reversal signal processing optimization, Wave Motiondoi:http://dx.doi.org/10.1016/j.wavemoti.2016.07.001.

[9] S. Dos Santos, S. Vejvodova, Z. Prevorovsky, Nonlinear signal processing for ultrasonic imaging of material complexity, Proc. Estonian Acad. Sci. 59 (2) (2010) 108–117.

[10] J. N. Reddy, An Introduction to the Finite Element Method, McGraw-Hill, New York, 2006.

[11] E. Jones, T. Oliphant, P. Peterson, et al., SciPy: Open source scientific tools for Python, http://www.scipy.org/, [Online; accessed 2014-12-08] (2001–).
URL http://www.scipy.org/

[12] A. H. Nielsen, Absorbing boundary conditions for seismic analysis in ABAQUS, in: Proc. of the 2006 ABAQUS Users' Conference, Cambridge, Massachusetts, 2006, pp. 23–25.

[13] Ultrasonic Velocity Table, http://www.advanced-ndt.co.uk/index_htm_files/Reference%20Chart%20-%20Velocity%20Chart.pdf, accessed: 2016/09/24.

[14] O. C. Zienkiewicz, R. L. Taylor, The Finite Element Method Fifth edition Volume 1: The Basis, Butterworth-Heinemann, 2000.

[15] O. C. Zienkiewicz, R. L. Taylor, The Finite Element Method Fifth edition Volume 2: Solid mechanics, Butterworth-Heinemann, 2000.

[16] T. A. Laursen, Computational Contact and Impact Mechanics: Fundamentals of Modeling Interfacial Phenomena in Nonlinear Finite Element Analysis, Springer Berlin Heidelberg, 2002.

[17] D. Xu, K. D. Hjelmstad, A New Node-to-Node Approach to Contact/Impact Problems for Two-Dimensional Elastic Solids Subject to Finite Deformation, Tech. rep., Newmark Structural Engineering Laborator y of Department of Civil and Environmental Engineering at the University of Illinois at Urbana-Champaign (May 2008).

[18] A. R. Mijar, J. S. Arora, Return Mapping Procedure for Frictional Force Calculation: Some Insights, Journal of Engineering Mechanics 131 (10) (2005) 1004–1012.

[19] A. Schutte, J. F. Dannenberg, Y. H. Wijnant, A. de Boer, An implicit and explicit solver for contact problems, in: Proceedings of ISMA2010 including USD2010, 2010, pp. 4081–4094.

[20] A. R. Mijar, J. S. Arora, An augmented Lagrangian optimization method for contact analysis problems, 1: formulation and algorithm , Struct Multidisc Optim 28 (2004) 99–112.

[21] A. Logg, K.-A. Mardal, G. Wells (Eds.), Automated Solution of Differential Equations by the Finite Element Method: The FEniCS Book (Lecture Notes in Computational Science and Engineering), Springer, 2012.

[22] M. Lints, FEM simulation video of TR-NEWS focusing on crack in CFRP, `http://homes.ioc.ee/lints/files/cracked_CF_TR-NEWS_foc3.mp4`, Accessed: 2017/02/01.